48. Photoconductors for X-Ray Image Detectors

Recent flat-panel X-ray imaging detectors have been shown to be able to replace present-day X-ray film/screen cassettes; they capture an X-ray image electronically and hence enable a clinical transition to digital radiography. This chapter critically discusses the material, transport and imaging detector properties (e.g., dark current) of several potential X-ray photoconductors and compares them with an ideal photoconductor for use in direct-conversion imaging detectors. The present chapter also considers various metrics of detector performances including sensitivity, detective quantum efficiency, resolution in terms of the modulation transfer function, image lag and ghosting; and examines how these metrics depend on the photoconductor, and detector structure and design.

The flat-panel X-ray image detector (sensor) concept is illustrated in Fig. 48.1 where X-rays passing through the patient's hand are incident on a sensor. The sensor converts the incident image to a digital image that can be sent to a computer and viewed on a monitor. Research over the past ten years [48.1] has indicated that the most practical flat-panel medical digital radiographic systems (mammography, chest radiography and fluoroscopy) are those based on a large-area integrated circuit or active matrix array (AMA). Flat-panel imagers incorporating active matrix arrays are called active matrix flat-panel imagers or AMFPI. Active matrix arrays using hydrogenated amorphous silicon (a-Si:H) thin-film transistors (TFTs) have been shown to be practical pixel-addressing systems for displays [48.2]. These a-Si:H arrays can be converted into X-ray-sensitive imaging devices by adding a thick (0.1–1 mm) X-ray-detecting medium, either a phosphor or a photoconductor. The physical form of the X-ray AMFPI is similar to a film/screen cassette and thus it will easily fit into current medical film/screen-based X-ray imaging systems. The X-ray image is stored and displayed on the computer almost immediately after the X-ray exposure. The stored image can be rapidly transmitted to remote locations for consultation and analysis. The dynamic range of recently developed AMFPI systems is much higher than film/screen-based imaging systems [48.3]. AMFPI are able to read out an entire image in 1/30 s, sufficiently rapid to perform fluoroscopy (real-time imaging) [48.4].

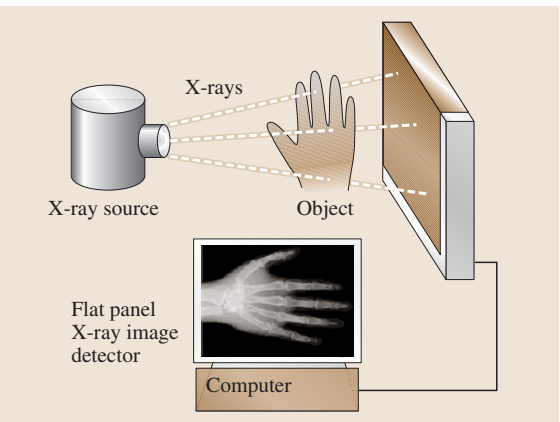

Fig. 48.1 Schematic illustration of an active matrix flat-panel imaging (AMFPI) system used for X-ray imaging

The active matrix array used for pixel addressing and readout in an AMFPI consists of many single pixels, each of which represents a corresponding pixel of the image. Each pixel collects charge proportional to the X-ray radiation that it receives. To generate this signal charge, either a phosphor converts the X-rays

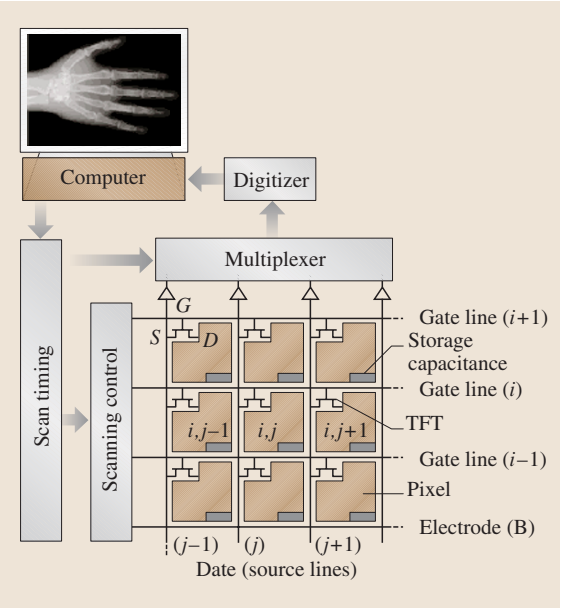

Fig. 48.2 Schematic diagram that shows some pixels of the active matrix array for use in X-ray AMFPI with self-scanned electronic readout. The charge distribution residing on the panel's pixels are read out by scanning the arrays row by row using peripheral electronics and multiplexing the parallel columns into a serial digital signal

to visible light, which in turn is detected with a pin photodiode at the pixel (indirect) or an X-ray photoconductor converts the incident X-rays to charge (direct) in one step. For both the indirect and direct conversion approaches, the latent image is a charge distribution residing on the array's pixels. The charges are read out by scanning the arrays row by row using peripheral electronics and multiplexing the parallel columns into a serial digital signal. This signal is then transmitted to a computer system for storage and display. Several manufacturers and academic researchers have used the indirect approach [48.5, 6]. However, we believe that the direct approach, due to its higher conversion gain, has the potential to produce systems superior in image quality to indirect conversion sensors and be both easier and cheaper to manufacture due to their simpler structure. This chapter considers only the direct-conversion X-ray imager and how its dark current, sensitivity, resolution and detective quantum efficiency (DQE) depend on the photoconductor and detector structure. This chapter also discusses essential photoconductor properties, charge transport and imaging properties of promising photoconductors.

Active matrix arrays allow a monolithic imaging system of large area (e.g. 40 cm × 40 cm) to be constructed. As for conventional integrated circuits, planar processing of the array through deposition and doping of lithographically masked individual layers of metals, insulators and semiconductors implement the design of active matrix arrays. In the future, even larger areas should become feasible if required. Millions of individual pixel electrodes in the matrix and are connected, as shown in Fig. 48.2. Each pixel has its own thin-film transistor (TFT) switch and storage capacitor to store image charges. The TFT switches control the image charge so that one line of pixels is activated electronically at a time. Normally, all the TFTs are turned off, permitting the latent image charge to accumulate on the array. The readout is achieved by external electronics and software controlling the state of the TFT switches. The active matrix array consists of $M \times N$ (e.g. 2480 × 3072) storage capacitors C_{ij} whose stored image charge can be read through properly addressing the TFT (i, j) via the gate (i) and source (j) lines. The charges read on each C_{ij} are converted to a digital image. The image readout technique is described by *Rowlands* and *Kasap* [48.7]. The readout is self-scanning in that no external means such as a laser are used. The scanning is part of the AMFPI electronics and software, thus permitting a truly compact device.

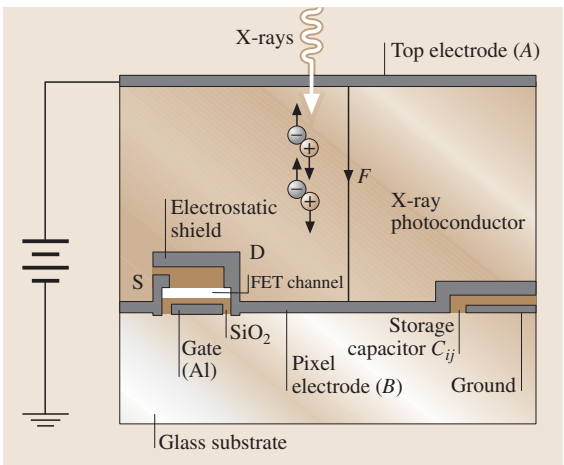

Fig. 48.3 Cross section of a single pixel (i, j) with a TFT switch. The top electrode (A) on the photoconductor is a vacuum-coated metal (e.g. Al). The bottom electrode (B) is the pixel electrode that is one of the plates of the storage capacitance (C_{ij}). (Not to scale—the TFT height is highly exaggerated)

To construct a direct-conversion X-ray AMFPI, a large-band-gap ($> 2\,\text{eV}$) high-atomic-number semiconductor or X-ray photoconductor (e.g., stabilized amorphous selenium, a-Se) layer is coated onto the active matrix array. An electrode (A) is subsequently deposited onto the photoconductor layer to facilitate the application of a biasing potential and, hence, an electric field F in the photoconductor layer as shown in Fig. 48.3. The biasing potential applied to the radiation receiving electrode A (top electrode) may be positive or negative, the selection of which depends on many factors discussed later in this chapter. The applied bias varies from a few hundred to several thousand Volts. The capacitance C_{pc} of the photoconductor layer over the pixel is in series with, and much smaller than, the pixel capacitance C_{ij} attached to the pixel electrode, so that most of the applied potential is dropped across the photoconductor and not across the pixel capacitance. The electron–hole pairs (EHPs) generated in the photoconductor by the absorption of X-ray photons travel along the field lines and are collected by the electrodes. If the applied bias voltage is positive, then electrons collect at the positive bias electrode and holes accumulate on the storage capacitor C_{ij}. Each pixel electrode carries an amount of charge Q_{ij} proportional to the amount of incident X-ray radiation in the photoconductor layer over that pixel, which can be read during self-scanning.

The selection of the photoconductor material for use in direct-conversion X-ray image detectors is currently an important research field in electronic materials. There are various competing semiconductors, such as amorphous (a-)Se, HgI_2, CdZnTe, PbI_2, PbO and TlBr. Detectors based on a-Se have already been developed and some have been commercialized for mammography, general radiography and fluoroscopy [48.8] with active areas as large as $43\,\text{cm} \times 43\,\text{cm}$. This chapter critically discusses charge-transport and imaging-detector properties (e.g., dark current and image lag) of these photoconductors and compares them with an ideal photoconductor for X-ray imaging detectors. The present chapter also examines various imaging characteristics of photoconductor-based X-ray AMFPIs, including sensitivity (S), detective quantum efficiency (DQE), resolution in terms of the modulation transfer function (MTF), image lag and ghosting. We examine how these characteristics depend not only on the photoconductor's charge-transport properties but also on the detector structure, i. e., the size of the pixel and the thickness of the photoconductor.

48.1 X-Ray Photoconductors

48.1.1 Ideal Photoconductor Properties

The performance of direct-conversion X-ray detectors depends critically on the selection and design of the photoconductor. It is therefore instructive to identify what constitutes a nearly ideal X-ray photoconductor to guide a search for improved performance or a better material. Ideally, the photoconductive layer should possess the following material properties:

1. Most of the incident X-ray radiation should be absorbed within a practical photoconductor thickness to avoid unnecessary patient exposure. This means that, over the energy range of interest, the absorption depth δ of the X-rays must be substantially less than the device layer thickness L. In other words, the quantum efficiency (η) should be high.
2. The photoconductor should have high intrinsic X-ray sensitivity, i. e., it must be able to generate as many collectable (free) electron–hole pairs (EHPs) as possible per unit of incident radiation. This means the amount of radiation energy required, denoted by $W_{\pm}$, to create a single free electron–hole pair must be as low as possible. Typically, $W_{\pm}$ increases with the band gap E_g of the photoconductor [48.9] and thus a low E_g is desired for maximum X-ray sensitivity.
3. There should be little bulk recombination of electrons and holes as they drift to the collection electrodes; EHPs are generated in the bulk of the photoconductor. Bulk recombination is proportional to the product of the concentration of holes and electrons, and typically it is negligible for clinical exposure rates (i. e. provided the instantaneous X-ray exposure is not too high).
4. There should be negligible deep trapping of EHPs, which means that, for both electrons and holes, the schubweg defined as $\mu\tau F \gg L$ where μ is the drift mobility, τ is the deep-trapping time (lifetime), F is the electric field and L is the photoconductor layer thickness. The schubweg is the mean distance a carrier drifts before it is trapped and unavailable for

conduction. The temporal responses of the X-ray image detector, such as lag and ghosting, depend on the rate of carrier trapping.

5. The diffusion of carriers should be negligible compared with their drift. This property ensures less time for lateral carrier diffusion and leads to better spatial resolution.
6. The dark current should be as small as possible, because it is a source of noise. This means the contacts to the photoconductor should be non-injecting and the rate of thermal generation of carriers from various defects or states in the band gap should be negligibly small (i. e. dark conductivity is practically zero). Small dark conductivity generally requires a wide-band-gap semiconductor, which conflicts with condition (2) above. The dark current should preferably not exceed 10–1000 pA/cm^2, depending on the clinical application [48.10].
7. The longest carrier-transit time, which depends on the smallest drift mobility, must be shorter than the image readout time and inter-frame time in fluoroscopy.
8. The properties of the photoconductor should not change with time because of repeated exposure to X-rays, i. e. X-ray fatigue and X-ray damage should be negligible.
9. The photoconductor should be easily coated onto the AMA panel (typically 30×30 cm and larger), for example, by conventional vacuum techniques without raising the temperature of the AMA to damaging levels (e.g., ≈ 300 °C for a-Si panels). This eliminates the possibility of using single-crystal materials that would require extended exposure to much higher temperature if they were to be grown directly onto the panel.
10. The photoconductor should have uniform characteristics over its entire area.
11. The temporal artifacts such as image lag and ghosting should be as small as possible. Lag is the carryover of image charge generated by previous X-ray exposures into subsequent image frames. The residual signal fractions following a pulsed X-ray irradiation are referred to as "image lag". Ghosting is the change of X-ray sensitivity of the X-ray image detector as a result of previous exposure to radiation. In the presence of ghosting, a shadow impression of a previously acquired image is visible in subsequent uniform exposures.

The large-area-coating requirement in (9) rules out the use of crystalline semiconductors, whose only practical production process is to grow large boules, which are subsequently sliced. Thus, only amorphous or polycrystalline (poly) photoconductors are currently practical for use in large-area X-ray imaging detectors. Amorphous selenium (a-Se) is one of the most highly developed photoconductors for large-area detectors due to its commercial use in photocopiers and laser printers as an electrophotographic photoreceptor [48.11]. In fact, the direct-conversion flat-panel imaging technology has been made possible by the use of two key elemental amorphous semiconductors: a-Si:H (used for TFTs) and a-Se (used for photoconductor layers). Although their properties are different, both can be readily prepared in large areas, which is essential for an X-ray imaging detector. Stabilized a-Se (a-Se alloyed with 0.2–0.5% As and doped with 10–40 ppm Cl) is currently the preferred photoconductor for clinical X-ray image sensors, because it can be quickly and easily deposited as a uniform film over large areas and it has an acceptable X-ray absorption coefficient, good charge-transport properties for both holes and electrons, and lower dark current than many competing polycrystalline layers [48.9, 10]. Flat-panel X-ray image detectors with an a-Se photoconductor have been shown to provide excellent images.

There has been active research to find potential X-ray photoconductors to replace a-Se in flat-panel image detectors because of the substantially higher $W_{\pm}$ and operating electric field of a-Se compared to other potential X-ray photoconductors [48.10, 12]. For example, the typical value of the electric field used in a-Se devices is 10 V/μm where the value of $W_{\pm}$ is about 45 eV; the value of $W_{\pm}$ is 5–6 eV for polycrystalline mercuric iodide (poly-HgI_2) and polycrystalline CdZnTe. The main drawback of polycrystalline materials is the adverse effects of grain boundaries in limiting charge transport and the nonuniform response of the sensor due to large grain sizes. Grain boundaries in the polycrystalline material are expected to create trapping levels within the band gap and introduce potential barriers between neighboring grains [48.13]. Another disadvantage of these polycrystalline detectors is the higher dark current compared to a-Se detectors. However, there have been efforts to improve the material properties and reduce the dark currents of polycrystalline HgI_2 and poly-CdZnTe-based image detectors [48.14, 15]. Recent experiments on large-area HgI_2, PbI_2, CdZnTe (< 10% Zn), and PbO polycrystalline X-ray photoconductive layers deposited on active matrix arrays have shown encouraging results [48.16–18]. A more detailed description of these three potential photoconductors for

direct-conversion AMFPIs is presented below along with TlBr.

48.1.2 Potential Photoconductors

The properties of an ideal photoconductor for X-ray image detectors have been discussed in the section above. In this section, important properties of potential photoconductors for X-ray image detectors are discussed and compared with the ideal case.

Amorphous Selenium (a-Se)

Stabilized a-Se can be easily coated as thick films (e.g., 100–1000 μm) onto suitable substrates by conventional vacuum deposition techniques and without the need to raise the substrate temperature beyond 60–70 °C (much below the damage threshold of the AMA, e.g., ≈ 300 °C for a-Si:H panels). Its amorphous state maintains uniform characteristics to a very fine scale over large areas. Stabilized a-Se, not pure a-Se, is used in X-ray sensors, because pure a-Se is thermally unstable and crystallizes over several weeks or months following manufacture. Crystalline Se is unsuitable as an X-ray photoconductor because it has a much lower dark resistivity and hence orders of magnitude larger dark current

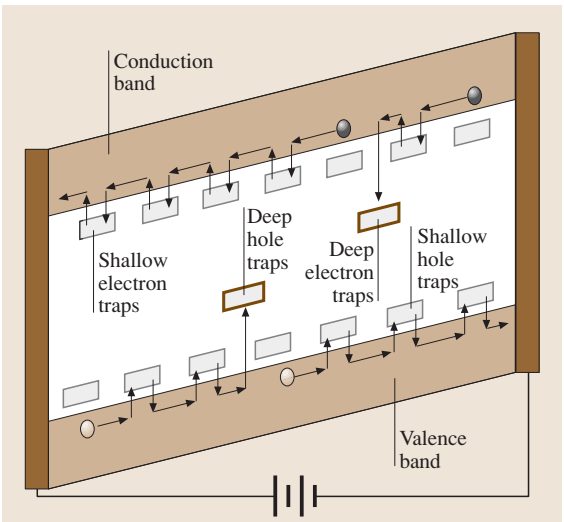

Fig. 48.4 Diagram illustrating the band gap of a photoconductor with an applied electric field that tilts the bands, encouraging drift of holes in the direction of the field and electrons counter to the field. Drift of both electrons and holes involves interactions with shallow and deep traps. Shallow traps reduce the drift mobility and deep traps prevent the carriers from crossing the photoconductor

than a-Se. Alloying pure a-Se with As (0.2–0.5% As) greatly improves the stability of the composite film and helps to prevent crystallization. However, it is found that the addition of As has an adverse effect on the hole lifetime because the arsenic introduces deep hole traps. If the alloy is doped with 10–20 parts per million (ppm) of a halogen (such as Cl), the hole lifetime is restored to its initial value. Thus, a-Se film that has been alloyed with 0.2–0.5% As (nominal 0.3% As) and doped with 10–20 ppm Cl is called stabilized a-Se. The density of a-Se is 4.3 g/cm^3 with an energy gap of $E_g \approx 2.1$–2.2 eV.

There are localized states in the so-called forbidden gap of a-Se. Some of these are located near the band edges (shallow traps), while some are located deep in the energy band (deep traps). Localized states are simply traps and are not extended throughout the material, but are localized in space (both shallow and deep) due to various structural defects that are stable at room temperature. Drift of both electrons and holes involves interactions with shallow and deep traps, as shown in Fig. 48.4. Shallow traps reduce the drift mobility; deep traps prevent the carriers from crossing the photoconductor. The effective drift mobility μ of carriers is the mobility μ_0 in the extended states reduced by the trapping and release events due to the presence of shallow traps,

$$\mu = \frac{\tau_c}{\tau_c + \tau_r}\mu_0 \,, \tag{48.1}$$

where τ_c and τ_r are the average capture and release times in the shallow-trap centers. The capture time represents the mean time that a mobile carrier drifts in the extended states before becoming trapped in a shallow-trap center. The release time is the mean time that a carrier remains in a trap before being released back into the extended states. Re-emission from a shallow trap is mostly dominated by thermally activated processes. The shallow-trap release time is relatively short and a typical carrier may experience many shallow capture and release events while traversing the detector thickness (100–1000 μm).

Although the nature of the shallow traps in a-Se has not been fully established, the drift mobilities of both holes and electrons are quite reproducible. The room-temperature effective hole mobility μ_h is independent of the preparation of the sample and has a value of $\approx 0.12\,\mathrm{cm}^2/\mathrm{V\,s}$, whereas the effective electron mobility μ_e is in the range 0.003–$0.006\,\mathrm{cm}^2/\mathrm{Vs}$ [48.12]. The hole drift mobility does not change with the addition of As or Cl. The value of μ_e decreases with the addition of

As to a-Se (e.g., in stabilized a-Se) but Cl doping does not affect it.

Once a carrier is caught in a deep trap, it will remain immobile until a lattice vibration gives it enough energy to be excited back into the extended states, where it can drift once again. The deep-trap release time is very long (minutes to hours), and a deeply trapped carrier is essentially permanently removed from conduction. Therefore, the carrier lifetime depends on the concentration of deep rather than shallow traps. The charge-carrier lifetimes vary substantially between different samples and depend on factors such as the source of a-Se material, impurities, and the preparation method. The electron lifetime τ_e is particularly sensitive to impurities in the a-Se source material. The hole lifetime τ_h drops rapidly with decreasing substrate temperature (temperature of the a-Se substrate during the evaporation process) whereas τ_e is unaffected. Increasing the As concentration in a-Se decreases τ_h and increases τ_e [48.19]. On the other hand, Cl doping increases τ_h and decreases τ_e. The typical lifetimes in stabilized a-Se are in the range 10–500 μs for holes and 100–1500 μs for electrons [48.12].

The fractional increase in the τ_e with As addition is greater than the drop in μ_e. Thus the electron range ($\mu_e\tau_e$) increases with As content. The effect of Cl doping on the carrier ranges ($\mu\tau$ products) is more pronounced than that of As doping. Thus, we can control both electron and hole ranges by appropriately choosing the relative amounts of As and Cl in a-Se.

The electron–hole-pair creation energy $W_\pm$ in a-Se has a strong dependence on electric field F but only a weak dependence on the X-ray photon energy E [48.20,21]. The quantity $W_\pm$ is decreased by increasing either F or E. $W_\pm$ at a given E in a-Se follows an empirical relation given by

$$W_\pm \approx W_\pm^0 + \frac{B(E)}{F^n}\,, \qquad (48.2)$$

where $B(E)$ is a constant that depends on E, $W_\pm^0$ is the saturated EHP creation energy (at infinite F), and n is typically in the range 0.7–1 [48.22]. The value of $W_\pm^0$ should be $2.2E_g + E_{phonon}$ [48.23], where E_{phonon} is the phonon energy. With $E_g \approx 2.1$ eV and $E_{phonon} < 0.5$ eV, we would expect that $W_\pm^0 \approx 5$ eV. The energetic primary electron generates many EHPs but only a certain fraction of these are free to drift and the rest recombine before they can contribute to the photocurrent. There are various possible explanations for the F dependence of the EHP creation energy. First, the simultaneously generated electron and its hole twin are attracted to each other by their mutual Coulombic force and may eventually recombine. This type of recombination is called geminate recombination (from Gemini–the twins). Another possible mechanism is columnar recombination that involves the recombination of nongeminate electrons and holes generated close to each other in the columnar track of the single high-energy electron (primary) created by the absorption of an X-ray. In both the geminate and columnar cases, the number of carriers escaping recombination should increase with increasing F, which acts to separate the oppositely charged carriers. The question of whether the F dependence of $W_\pm$ in a-Se is dominated by geminate or columnar recombination has not been fully resolved and is currently an area of research [48.23,24]. However, the energy dependence of $W_\pm$ is better understood. It decreases slowly with increasing photon energy in the diagnostic [48.20] and megavolt range [48.25]. The total change in $W_\pm$ from 20 keV to 6 MeV is of the order of three. This appears to be due to a reduction of recombination with increase in energy. The rate of deposition of energy per unit distance traveled by a primary electron decreases as a function of energy, decreasing the density of EHPs in the column around it. This is expected to reduce columnar recombination–as is seen. Thus it appears that at low energies the contribution from columnar recombination is approximately twice that from geminate, but at high enough energy the columnar effect is reduced to zero. The typical value of the F used in a-Se devices is 10 V/μm where the value $W_\pm$ is 35–55 eV over the diagnostic beam energy (12–120 keV) and ≈ 15 eV at megavolt energies.

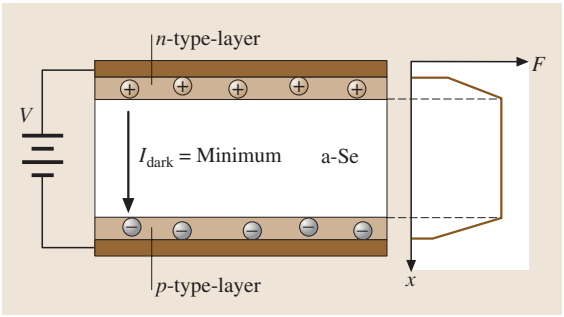

Fig. 48.5 A multilayer pin-type a-Se device structure for blocking dark current

The dark resistivity of a-Se is $\approx 10^{14}\,\Omega$ cm. The bulk-induced dark current in a-Se detectors is within the acceptable limit ($< 1\,\text{nA/cm}^2$) for $F \le 20\,\text{V/μm}$. However, the injected dark current for metal/a-Se/metal single-layer structures depends on the nature of the metal/a-Se contacts and nonlinearly on F. It has

however been possible to reduce the dark current to a negligible level in multilayer a-Se structures, e.g., ($< 0.1\,\mathrm{nA/cm^2}$ at F as high as $20\,\mathrm{V/\mu m}$ [48.26]) by use of blocking contacts. A pin (p-type–intrinsic–n-type) a-Se structure is shown in Fig. 48.5, where the thickness of both the p and n blocking contact layers is a few microns. These p- and n-layers are appropriately doped to serve as unipolar conducting layers that easily trap electrons and holes, respectively, but allow the transport of oppositely charged carriers. The rate of emission of these deeply trapped carriers is so small that there is no significant current injection into the bulk a-Se layer. With these n- and p-layers, the F at the metal electrodes is sufficiently small to minimize charge injection from the contacts, which substantially reduces the dark current.

The image lag in a-Se detectors is under 2% after 33 ms and less than 1% after 0.5 s in the fluoroscopic mode of operation [48.27]. Therefore, image lag in a-Se detectors is considered to be negligible. The pixel-to-pixel sensitivity variation is also negligible in a-Se detectors. The presampling MTF of these detectors is almost equal to the theoretical MTF (sinc function) determined by the pixel aperture [48.28].

Mercuric Iodide (HgI_2)

Poly-HgI_2 has been used as a photoconductor layer in X-ray image detectors. It has been prepared by either physical vapor deposition (PVD) or screen printing (SP) from a slurry of HgI_2 crystals using a wet particle-in-binder process [48.16]. There appears to be no technological barrier to preparing large-area layers, and direct-conversion X-ray AMFPI of $20\times25\,\mathrm{cm^2}$ (1536×1920 pixels) and $5\times5\,\mathrm{cm^2}$ (512×512 pixels) size have been demonstrated using PVD [48.16] and SP poly-HgI_2 layers. The prototype HgI_2 sensors can potentially be used for mammographic, fluoroscopic or radiographic imaging. There has been active research to improve the material properties of poly-HgI_2-based image detectors including improving the nonuniformity by reducing the grain size. The band-gap energy $E_g = 2.1\,\mathrm{eV}$, the ionization energy $W_\pm \approx 5\,\mathrm{eV}$ and the density of poly-HgI_2 is $6.3\,\mathrm{g/cm^3}$. The resistivity of this material is $\approx 4\times10^{13}\,\Omega\,\mathrm{cm}$ [48.29].

The HgI_2 layer is deposited onto either conductive [indium-tin-oxide- (ITO) or gold-coated] glass plates or a-Si TFT arrays. HgI_2 tends to react chemically with most metals; hence a thin blocking layer (typically, $\approx 1\,\mu\mathrm{m}$ layer of insulating polymer) is used between the HgI_2 layer and the pixel electrodes to prevent the reaction and also to reduce the dark current. The HgI_2 layer thickness varies in the range 100–500 μm and the grain size is 20–60 μm. Several hundred angstroms of palladium (Pd) or Au are deposited (by direct evaporation) on top of the HgI_2 layer followed by a polymer encapsulation layer to form a bias electrode.

The dark current of HgI_2 imagers increases superlinearly with the applied bias voltage. For PVD HgI_2 detectors the dark current depends strongly on the operating temperature. It increases by a factor of about two for each 6 °C of temperature rise. It is reported that the dark current varies from $\approx 2\,\mathrm{pA/mm^2}$ at 10 °C to $\approx 180\,\mathrm{pA/mm^2}$ at 35 °C at $F = 0.95\,\mathrm{V/\mu m}$, which is not desirable for medical imagers (the maximum dark current for medical imaging should be $< 10\,\mathrm{pA/mm^2}$). Therefore, PVD HgI_2 imagers should be operated at relatively low bias (preferably less than $\approx 0.5\,\mathrm{V/\mu m}$) and relatively low temperature (< 25 °C). The dark current in the SP sample is an order of magnitude smaller than in the PVD sample and more stable against temperature variation. It is possible to keep the dark current below $10\,\mathrm{pA/mm^2}$ at temperatures up to 35 °C and $F = 1\,\mathrm{V/\mu m}$. A major disadvantage of SP detectors is that they show 2–4 times less sensitivity compared to PVD detectors.

Electrons have much longer range than holes in HgI_2 and thus the receiving electrode is negatively biased to obtain a higher sensitivity. The $\mu_e\tau_e$ for electrons in the SP HgI_2 is in the range 10^{-6}–$10^{-5}\,\mathrm{cm^2/V}$ [48.16, 30], and $\mu_e\tau_e$ in the PVD sample is about an order of magnitude greater. Recently it was reported that $\mu_e\tau_e$ in PVD HgI_2 is in the range $\sim 10^{-5}$–$10^{-4}\,\mathrm{cm^2/V}$, which is almost equal to that of single-crystal HgI_2 [48.14, 31]. The reason is that the PVD HgI_2 layer grows in a columnar structure perpendicular to the substrate. Thus a charge carrier may drift along a column without having to pass through grain boundaries, where it would encounter excess trapping and/or recombination. Samples with larger grain sizes may have fewer grain-boundary defects. Hence there is a trend of increasing $\mu_e\tau_e$ with grain size in the PVD samples. However, this trend is not observed in the SP sample, which indicates another mechanism is responsible for its low $\mu_e\tau_e$. Larger grain sizes may cause nonuniform sensor response. The grain sizes must be much smaller than the pixel size to get a uniform response. $\mu_h\tau_h$ in poly-HgI_2 is of the order $\approx 10^{-7}\,\mathrm{cm^2/V}$ [48.30].

Two important drawbacks of polycrystalline sensors are the image lag and the pixel-to-pixel sensitivity variation or nonuniform response. The lowest image-lag characteristics reported are ≈ 7% first-frame lag, ≈ 0.8% after 1 s and ≈ 0.1% at 3 s in fluoroscopic

mode (15 frames/s). The pixel-to-pixel sensitivity variation reduces the dynamic range of the imagers. The relative standard deviation of the sensitivity (standard deviation/average value) in the latest HgI_2 AMFPI is $\approx 10\%$. It is reported that HgI_2 image detectors with smaller grain sizes show good sensitivity and also an acceptably uniform response. The presampling MTF of these detectors is almost equal to the theoretical MTF (sinc function) determined by the pixel aperture.

Cadmium Zinc Telluride (CdZnTe)

CdZnTe (< 10% Zn) polycrystalline film has been used as a photoconductor layer in X-ray AMFPI. CdZnTe is commonly called CZT. Although CZT can be deposited on large areas, direct-conversion AMFPI of only $7.7\times7.7\,cm^2$ (512×512 pixels) have been demonstrated using polycrystalline CZT (poly-CZT). The CZT layer thickness varies in the range 200–500 μm. Temporal lag and nonuniform response were noticeable in early CZT sensors. Large and nonuniform grain sizes are believed to be responsible for the temporal lag and nonuniform response of the sensor. Recent studies show that Cl doping makes a finer, more uniform grain structure [48.15]. The ionization energy $W_{\pm} \approx 5\,eV$, and the density of band gap $Cd_{0.95}Zn_{0.05}Te$ is $5.8\,g/cm^3$. The band gap energy E_g of $Cd_{0.95}Zn_{0.05}Te$ is 1.7 eV and the resistivity of this material is $\approx 10^{11}\,\Omega$ cm [48.32].

Typically CZT is first coated onto an inert substrate and then attached to the active matrix array. The advantage of this technique is that the electrical properties and hence imaging performances of the detector can be optimized without causing any thermal or chemical damage to the TFT array. The CZT film is deposited by the close-spaced sublimation method [48.33] onto an alumina (Al_2O_3) substrate coated with ITO, which forms the bias (top) electrode. A cross section of the poly-CZT detector is shown in Fig. 48.6. The several-microns-thick ZnTe layer acts as a barrier to electron injection and hence suppresses dark current under the negative bias. This ZnTe layer is omitted for the positive bias. Conducting resin bumps on the pixel electrodes connect each pixel to the CZT layer.

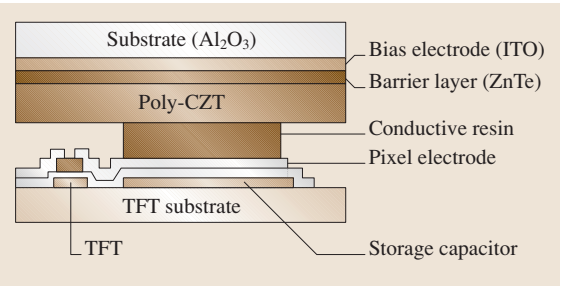

Fig. 48.6 Cross section of the polycristalline CZT detector structure (after *Tokuda* et al. [48.15])

Introduction of Zn into the CdTe lattice increases the band gap, decreases the conductivity and hence reduces the dark current. In CZT μ_h decreases with increasing Zn concentration whereas μ_e remains nearly constant. Again, addition of Zn to CdTe increases lattice defects and hence reduces carrier lifetimes. The poly-CZT has a lower density, which results in a lower quantum efficiency η than its single-crystal counterpart. Although (for a detector of given thickness) X-ray sensitivity in CZT detectors is lower than in CdTe detectors, the CZT detectors show a better signal-to-noise ratio and hence give a better DQE. The measured sensitivities are higher than a-Se.

The dark current of $Cd_{0.95}Zn_{0.05}Te$ imagers increases almost linearly with F and is $\approx 70\,pA/mm^2$ at $F = 0.25\,V/\mu m$ [48.17], which makes it unsuitable for applications requiring long exposure times. The dark current would be expected to decrease with increasing Zn concentration due to the increased E_g. This has in fact, been demonstrated [48.15], i. e., the dark current in $Cd_{0.92}Zn_{0.08}Te$ sensors is $40\,pA/mm^2$ at $F = 0.4\,V/\mu m$.

The mobility–lifetime products of both electrons and holes in poly-CZT are less than in single-crystal CZT. The values of $\mu\tau$ in single-crystal $Cd_{0.9}Zn_{0.1}Te$ are in the range 10^{-4}–$10^{-3}\,cm^2/V$ (electrons) and 10^{-6}–$10^{-5}\,cm^2/V$ (holes) [48.34]. But the values of $\mu\tau$ in poly-$Cd_{0.95}Zn_{0.05}Te$ are $\approx 2\times10^{-4}\,cm^2/V$ (electrons), and $\approx 3\times10^{-6}\,cm^2/V$ (holes) [48.35, 36]. Since $\mu_e\tau_e \gg \mu_h\tau_h$ in CZT, negative bias to the radiation-receiving electrode is the preferred choice for better sensitivity and temporal response.

The relative standard deviation of the sensitivity (standard deviation/average value) in the latest CZT AMFPI is $\approx 20\%$ [48.15]. The image-lag characteristics reported are $\approx 70\%$ first-frame lag, $\approx 20\%$ after three frames and 10% at 1 s in fluoroscopic mode (30 frames/s). In single-pulse radiographic mode the first-frame lag is less than 10% [48.15]. The longer image-lag characteristics of CZT sensors in fluoroscopic mode imply that it is not yet suitable for fluoroscopic applications. The presampling MTF of CZT detector is ≈ 0.3 (150-μm pixel size) at the Nyquist frequency f_N (theoretical MTF, sinc function, is ≈ 0.64 at $f_N = 3.3$ line pairs per mm), where the MTF of CsI imagers is less than 0.2 [48.17].

Lead Iodide (PbI_2)

PbI_2 polycrystalline photoconductive layers have been prepared using PVD at a substrate temperature of 200–230 °C. A deposition of several hundred angstroms of palladium (Pd) is used to form a top electrode. Grains are described as hexagonal platelets with the longest dimensions being 10 μm or less. The platelets grow perpendicular to the substrate, producing films that are less dense (3–5 g/cm^3) than bulk crystalline material (6.2 g/cm^3). There appears to be no technological barrier to preparing large-area layers, and direct-conversion AMFPI of $20\times25\,cm^2$ size (1536×1920 pixels) have been demonstrated [48.37]. Coating thickness varies in the range 60–250 μm and prototype PbI_2 imagers have been used for radiographic imaging [48.37]. The band-gap energy $E_g = 2.3$ eV, and the ionization energy $W_\pm \approx 5$ eV. The resistivity of this material is in the range 10^{11}–10^{12} Ω cm.

Lead iodide detectors have a very long image-lag decay time. The image lag depends on the exposure history. The image-lag characteristics reported are ≈ 75% first-frame lag, ≈ 15% after 3 s in fluoroscopic mode (15 frames/s), whereas in single-pulse radiographic mode the first-frame lag is less than 50% and drops below 1% within 1 s [48.37]. The long image-lag characteristics of PbI_2 in fluoroscopic mode imply that it is unsuitable for fluoroscopic applications.

The dark current of PbI_2 imagers increases sublinearly with the applied bias voltage. The dark current is in the range 10–50 pA/mm^2 at $F = 0.5$ V/μm, much higher than PVD HgI_2 detectors, making it unsuitable for long-exposure-time applications. The presampling MTF is ≈ 0.35 (127 μm pixel size) at f_N (theoretical MTF, sinc function, is ≈ 0.64 at $f_N = 3.93$ lp/mm), where the MTF of CsI imagers is less than 0.2 [48.37]. The resolution of PbI_2 imagers is acceptable but slightly worse than that of HgI_2 imagers. Also, the X-ray sensitivity of PbI_2 imagers is lower than that of HgI_2 imagers. The pixel-to-pixel sensitivity variation in PbI_2 imagers is substantially lower.

The $\mu\tau$ product of holes and electrons in PVD PbI_2 are $1.8\times10^{-6}\,cm^2/V$ and $7\times10^{-8}\,cm^2/V$, respectively [48.37]. μ_h in poly-PbI_2 is in the range 0.02–0.15 cm^2/Vs whereas μ_h in single-crystal PbI_2 is 2 cm^2/V s [48.38]. This indicates that μ_h in poly-PbI_2 is controlled by shallow traps, probably introduced at the grain boundaries.

Lead Oxide (PbO)

The large-area deposition requirement is compatible with the use of polycrystalline PbO (poly-PbO) film as a photoconductor layer in AMFPI. Direct-conversion flat-panel X-ray imagers of $18\times20\,cm^2$ (1080×960 pixels) from a poly-PbO with film thicknesses of ≈ 300 μm have been demonstrated [48.18]. One advantage of PbO over other X-ray photoconductors is the absence of heavy-element K-edges for the entire diagnostic energy range up to 88 keV, which suppresses additional noise and blurring due to the K-fluorescence. The ionization energy $W_\pm \approx 8$ eV and the density of poly-PbO is 9.6 g/cm^3. The band-gap energy E_g of PbO

Table 48.1 Material properties

Photoconductor, state and preparation	E_g (eV)	$W_\pm$ (eV)	Density (g/cm^3)	Resistivity (Ω cm)	Electrons $\mu_e(cm^2/Vs)$, $\mu_e\tau_e(cm^2/V)$	Holes $\mu_h(cm^2/Vs)$ $\mu_h\tau_h(cm^2/V)$
Stabilized a-Se, vacuum deposition	2.1–2.2	≈ 45 at 10 V/μm	4.3	10^{14}–10^{15}	$\mu_e = 0.003$–0.006 $\mu_e\tau_e = 0.3\times10^{-6}$–$10^{-5}$	$\mu_h = 0.12$ $\mu_h\tau_h = 10^{-6}$–6×10^{-5}
HgI_2, polycrystalline, PVD	2.1	5	6.3	$\approx 4\times10^{13}$	$\mu_e = 88$ $\mu_e\tau_e \approx 10^{-5}$–$10^{-4}$	$\mu_h = 3$–4 $\mu_h\tau_h \approx 10^{-6}$
HgI_2, polycrystalline, SP	2.1	5	6.3	$\approx 4\times10^{13}$	$\mu_e\tau_e \approx 10^{-6}$–$10^{-5}$	$\mu_h\tau_h \approx 10^{-7}$
$Cd_{0.95}Zn_{0.05}Te$, polycrystalline, vacuum deposition	1.7	5	5.8	$\approx 10^{11}$	$\mu_e\tau_e \approx 2\times10^{-4}$	$\mu_h\tau_h \approx 3\times10^{-6}$
PbI_2, polycrystalline, PVD	2.3	5	3–5	10^{11}–10^{12}	$\mu_e\tau_e = 7\times10^{-8}$	$\mu_h = 0.02$–0.15 $\mu_h\tau_h \approx 2\times10^{-6}$
PbO, polycrystalline, vacuum deposition	1.9	8–20	9.6	7–10×10^{12}	$\mu_e\tau_e \approx 5\times10^{-7}$	?
TlBr, polycrystalline	2.7	6.5	7.5	$\approx 5\times10^{9}$ at 20 °C	?	$\mu_h\tau_h \approx 1.5\times10^{-6}$

Table 48.2 Imaging properties

Photoconductor, state and preparation	Typical operating F (V/μm)	Dark current (pA/mm^2)	Lag (fluoroscopic mode of operation)	Uniformity/sensitivity variation (standard deviation/average value)
Stabilized a-Se, single layer	≈ 10	< 10 up to $F = 20$ V/μm	< 2% after 33 ms	Negligible
Stabilized a-Se, multilayer (PIN or NIP)	≈ 10	< 1 up to $F = 20$ V/μm	< 2% after 33 ms	Negligible
HgI_2, polycrystalline, PVD	≈ 0.5	≈ 6 at $F = 0.5$ V/μm	≈ 7% after 66 ms	≈ 10%
HgI_2, polycrystalline, SP	≈ 1.0	≈ 8 at $F = 1.0$ V/μm	≈ 7% after 66 ms	≈ 10%
$Cd_{0.95}Zn_{0.05}Te$. polycrystalline	≈ 0.25	≈ 25 at $F = 0.25$ V/μm	≈ 70% after 33 ms	≈ 20%
PbI_2, polycrystalline, PVD	≈ 0.5	10–50 at $F = 0.5$ V/μm	≈ 75% after 66 ms	?
PbO, polycrystalline	≈ 1.0	40 at 3 V/μm field	3–8% after 1 s	?
TlBr, polycrystalline	≈ 1.0	?	?	?

is 1.9 eV and the resistivity of this material is in the range $(7–10)\times10^{12}$ Ω cm [48.18].

Lead oxide photoconductive polycrystalline layers have been prepared by thermal evaporation in a vacuum chamber at a substrate temperature of ≈ 100 °C. An evaporated layer of Al, Au or Pd was used to form a top electrode of thickness 100–200 nm [48.39]. The PbO layer consists of very thin platelets of a few microns thickness and has a density of ≈ 50% of the single-crystal density. PbO slowly degrades if it is exposed to air under normal ambient temperature but a few hours exposure is acceptable. However, in the long term PbO reacts with water and CO_2 causing an increase in dark current and a decrease in X-ray sensitivity. Therefore, a polymer or a semiconductor (e.g., doped a-Se) passivation layer is used to prevent exposure to the atmosphere. This is usually placed between the photoconductor layer and the top metal electrode. The passivation layer avoids degradation of the PbO layer and reduces the dark current [48.39]. The dark current in PbO sensors is ≈ 40 pA/mm^2 at $F = 3$ V/μm [48.18]. $\mu_e\tau_e$ in poly-PbO is $\approx 5\times10^{-7}$ cm^2/V [48.18]. The lag signal in fluoroscopic mode is in the range 3–8% after 1 s. The presampling MTF of PbO detector is ≈ 0.5 (184 μm pixel size) at f_N (theoretical MTF, sinc function, is ≈ 0.64 at $f_N = 2.72$ lp/mm) [48.18].

Thallium Bromide (TlBr)

Polycrystalline thallium bromide (poly-TlBr) has not yet been used in an AMFPI but has been used in a large-area (9-inch-diameter) direct-conversion detector called an X-ray-sensitive electron-beam image tube (XEBIT). The operational principle of the XEBIT is similar to the standard light-sensitive vidicon that was utilized extensively in the commercial television industry. The XEBIT can replace an X-ray image intensifier coupled to a video camera using relay lenses with a single direct-conversion device [48.40]. The typical TlBr layer thickness is 300 μm.

The ionization energy $W_\pm \approx 6.5$ eV and the relative dielectric constant of TlBr is 33. The band-gap energy E_g of TlBr is 2.7 eV and its resistivity is $\approx 5\times10^9$ Ω cm under ambient conditions. At room temperature the dominant contribution to the dark current is ionic conductivity [48.40]. The ionic conductivity has an exponential dependence on temperature; the conductivity decreases by an order of magnitude for every 19 °C temperature decrease. Therefore, the dark current can be greatly decreased by Peltier cooling. $\mu_h\tau_h$ in TlBr is $\approx 1.5\times10^{-6}$ cm^2/V [48.40].

48.1.3 Summary and the Future

The material and imaging properties of potential photoconductors for X-ray image detectors are summarized in Tables 48.1 and 48.2. Stabilized a-Se is currently the best choice of photoconductor for clinical X-ray image detectors. The next closest competitor is the poly-HgI_2 imagers, which show excellent sensitivity, good resolution, and acceptable dark current, homogeneity and lag characteristics. However, the long-term stability of HgI_2 imagers has not been as thoroughly studied as

stabilized a-Se sensors. Both the dark current and the image-lag characteristics of CZT, PbI_2 and PbO detectors are worse than those of HgI_2 sensors. However, the X-ray detectors made with CZT photoconductive layers should be mechanically and chemically more stable than HgI_2-based detectors. The main drawback of a-Se detectors is its low conversion gain, which particularly affects the imaging sensor performance at low exposure. This can be overcome by utilizing the avalanche multiplication technique in the a-Se layer [48.41] and/or using on-pixel amplification [48.2]. However, further research is necessary to demonstrate basic operation as well as to examine the long-term stability of sensors utilizing these techniques. The main drawbacks of polycrystalline sensors are the image lag and the nonuniform response. Making smaller, finer and more uniform grain size in polycrystalline sensors may overcome these drawbacks.

48.2 Metrics of Detector Performance

X-ray sensitivity, resolution in terms of modulation transfer function (MTF), detective quantum efficiency (DQE), image lag and ghosting are often considered as the metrics of imaging performance. For most practical applications, the spatial-frequency-dependent (f-dependent) detective quantum efficiency, DQE(f), is the appropriate metric of overall system performance and is unity at all f for an ideal detector. The detector performance depends critically on the photoconductor material properties such as the mobility, carrier trapping (both shallow and deep), EHP creation energy, X-ray attenuation and absorption coefficients. The material properties such as carrier mobility, EHP creation energy, X-ray attenuation and absorption coefficients in a well-defined photoconductor are almost constant, but the carrier lifetimes may vary from sample to sample. Shallow and deep trapping are particularly responsible for image lag and ghosting, respectively. The effects of charge-transport properties ($\mu\tau$) and the attenuation coefficient of photoconductor materials on the detector performance depends on L and F through the following normalized parameters,

$$
\begin{aligned}
\Delta &= \text{normalized attenuation depth} \\
&\quad (\text{attenuation depth/thickness}) \\
&= 1/(\alpha L)\,, \\
x_e &= \text{normalized electron schubweg} \\
&\quad (\text{electron schubweg per unit thickness}) \\
&= \mu_e \tau_e F/L\,, \text{and}\,, \\
x_h &= \text{normalized hole schubweg} \\
&\quad (\text{hole schubweg per unit thickness}) \\
&= \mu_h \tau_h F/L\,.
\end{aligned}
$$

where α is the linear attenuation coefficient of the photoconductor, $\mu_{e(h)}$ is the mobility and $\tau_{e(h)}$ is the deep-trapping time (lifetime) of electrons (holes). Equivalently, x_e and x_h are the normalized carrier lifetimes (carrier lifetimes per unit transit time) for electrons and holes, respectively. The ranges of these normalized parameters for the three most promising photoconductive (a-Se, poly-HgI_2 and poly-CZT) X-ray image detectors are given in Table 48.3. The combined effects of charge-transport properties (mobility and carrier lifetime), operating conditions (F and E), photoconductor thickness, and the attenuation coefficient of the photoconductor material on the imaging characteristics (X-ray sensitivity, DQE, MTF and ghosting) are examined in the following sections. It must be emphasized that the photoconductor thickness L and the operating field F are as important to the overall performance of the detector as the material properties of the photoconductor itself, a point that will become apparent in the results presented in this chapter.

48.2.1 X-Ray Sensitivity

The X-ray sensitivity (S) of a photoconductive detector is defined as the collected charge per unit area per unit exposure of radiation and is considered an important performance measure for a superior image. High S permits the use of low detector radiation-exposure levels which also increases the dynamic range of the AMPFI. The selection of the X-ray photoconductor is highly influenced by the value of S.

The value of S can be considered to arise in terms of three controlling factors: firstly, the amount of radiation actually absorbed from the incident radiation that is useful for the generation of electron–hole pairs (EHPs), which is characterized by the quantum efficiency η of the detector and depends on the value of α of the photoconductor and L through $\eta = 1 - e^{-\alpha L}$, where the value of α is X-ray photon-energy-dependent; secondly, the generation of EHPs by X-ray interactions, which is char-

Table 48.3 The values of Δ, x_e and x_h for a-Se, poly-HgI_2 and poly-CZT detectors

Photoconductor	$\mu_e\tau_e$ (cm^2/V) $\mu_h\tau_h$ (cm^2/V)	F (V/μm)	E (keV)	L (mm)	x_e	x_h	Δ
Stabilized a-Se	$\mu_e\tau_e = 0.3\times10^{-6}$–$10^{-5}$ $\mu_h\tau_h = 10^{-6}$–6×10^{-5}	≈ 10	20 60	0.2 1.0	1.5–50 0.3–10	5–300 1–60	0.24 0.98
Poly-HgI_2	$\mu_e\tau_e \approx 10^{-6}$–$10^{-5}$ $\mu_h\tau_h \approx 10^{-7}$	0.5–1	20 60	0.15 0.3	0.7–7 0.35–3.5	≈ 0.1 ≈ 0.05	0.21 0.85
Poly-$Cd_{0.95}Zn_{0.05}Te$	$\mu_e\tau_e \approx 2\times10^{-4}$ $\mu_h\tau_h \approx 3\times10^{-6}$	≈ 0.25	20 60	0.3 0.3	≈ 17 ≈ 17	≈ 0.25 ≈ 0.25	0.26 0.89

acterized by the value of $W_\pm$ of the photoconductor and the average absorbed energy (E_{ab}) per attenuated X-ray photon of energy E, where $W_\pm$ depends on the material properties of the photoconductor, and E_{ab} depends on the incident X-ray photon energy [48.42] and the material properties; and thirdly, how much of the X-ray generated charge is actually collected in the external circuit. This is characterized by the charge-carrier drift mobilities (μ) and lifetimes (τ), the applied F and L.

The S of an X-ray image detector can be normalized with respect to the maximum sensitivity (S_0) that would arise if all the incident radiation were absorbed and all the liberated carriers were collected. Neglecting secondary photon interactions, the expression for S_0 is [48.22]

$$S_0 = \left(\frac{5.45\times10^{13}e}{(\alpha_{air}/\rho_{air})W_\pm}\right)\left(\frac{\alpha_{en}}{\alpha}\right), \qquad (48.3)$$

where e is the elementary charge, α_{en} is the energy absorption coefficient of the photoconductor, while α_{air} and ρ_{air} are the energy absorption coefficient of air and its density. If $W_\pm$ is expressed in eV, α_{air}/ρ_{air} is in cm^2/g and exposure in (48.3) is in Roentgens, then S_0 is in units of C/cm^2R. Thus S_0 is a constant that depends on E and the material properties of the photoconductor, since $W_\pm$ is a material property which can usually be taken as constant for a given material. For those materials (e.g., a-Se) that have a significant F- and/or E-dependent $W_\pm$, then S_0 depends on F and/or E.

The quantity $s = S/S_0$ takes into account the X-ray absorption and charge-transport effects and is called the charge-collection and absorption-limited normalized sensitivity. It should be emphasized that s is a quantity that is determined by the X-ray absorption profile, photoconductor thickness and the charge-collection efficiency. The s of an X-ray image detector considering small signal operation, a constant μ and a single deep-trapping time (lifetime) τ for each type of carrier (holes and electrons) and neglecting carrier diffusion is given by [48.43],

$$\begin{aligned} S/S_0 &= x_h\left[\left(1-e^{-\frac{1}{\Delta}}\right)+\frac{1}{\Delta/x_h-1}\left(e^{-\frac{1}{x_h}}-e^{-\frac{1}{\Delta}}\right)\right] \\ &\quad + x_e\left[\left(1-e^{-\frac{1}{\Delta}}\right)-\frac{1}{\Delta/x_e+1}\left(1-e^{-\frac{1}{\Delta}-\frac{1}{x_e}}\right)\right] \\ &= s_h(x_h,\Delta)+s_e(x_e,\Delta) = s(x_h,x_e,\Delta) \end{aligned} \qquad (48.4)$$

where subscripts h and e refer to holes and electrons respectively.

The two square brackets on the right-hand side of the normalized sensitivity s expression (48.4) represent the relative contributions of hole and electron transport to the overall sensitivity for a given Δ. It is assumed in (48.4) that the radiation receiving side of the detector is biased positively. If the bias polarity is reversed, then x_e and x_h must be interchanged. The expression in (48.4) applies for incident radiation that is monoenergetic and has to be appropriately integrated over the radiation spectrum of a practical polyenergic X-ray source by considering the X-ray photon-energy-dependent terms $W_\pm$, α and α_{en}. Equation 48.4 applies to an isolated photoconductor sandwiched between two large-area parallel-plate electrodes (small pixel effects are excluded) [48.44] and operating under a constant E (small signal case). An excellent fit of (48.4) to experimental data on poly-HgI_2 is given in [48.30].

The value of s is always less than unity since S for a photoconductor of finite thickness in which carrier collection is not perfect is always less than S_0. Note that $s(x_h, x_e, \Delta) = s_h + s_e = 1$ when all the incident radiation is absorbed and all the charges are collected, i. e., x_h, $x_e \gg 1$ and $\Delta \ll 1$. The sensitivity is then simply S_0 and is controlled by $W_\pm$.

The sensitivity is mainly controlled by the charges that have the same polarity as the bias on the radiation-receiving electrode: holes for positive bias and electrons for negative bias [48.30, 43]. The extent of the disparity between s_h and s_e depends on Δ. The disparity

Table 48.4 X-ray sensitivity of a-Se, poly-HgI_2 and poly-CZT detectors using the normalized parameters from Table 48.3

Photoconductor	E (keV)	S_0 ($\mu C/cm^2R$)	$s = S/S_0$		S ($\mu C/cm^2R$)	
			Positive bias	Negative bias	Positive bias	Negative bias
Stabilized a-Se	20	0.244	0.9–0.98	0.8–0.98	0.22–0.24	0.2–0.24
	60	5.37	0.39–0.64	0.35–0.62	2.1–3.38	1.88–3.35
Poly-HgI_2	20	2.75	0.25–0.29	0.53–0.81	0.7–0.81	1.46–2.24
	60	38.54	0.15–0.3	0.21–0.4	6.76–11.21	8.18–15.6
Poly-$Cd_{0.95}Zn_{0.05}Te$	20	3	≈ 0.456	≈ 0.85	≈ 1.37	≈ 2.55
	60	35.87	≈ 0.41	≈ 0.51	≈ 14.69	≈ 18.12

is stronger for lower Δ, which can be understood by noting that electron and hole generation do not occur uniformly throughout the thickness of the sample but rather it is more effective closer to the radiation receiving electrode. An advantage of a-Se detectors is that both x_e and x_h are much greater than one, which is not the case for other photoconductors, as shown in Table 48.3. Therefore, charge collection in a-Se detectors is close to unity and the normalized sensitivity is controlled by the quantum efficiency of the detector. The S and s of different photoconductive detectors using the normalized parameters from Table 48.3 are given in Table 48.4. The values of $W_\pm$ for a-Se were taken from the work of *Blevis* et al. [48.20]. At $F = 10\,V/\mu m$, $W_\pm = 42.5$ and 46 eV for X-ray photon energies of 60 and 20 keV, respectively. The maximum X-ray sensitivity S_0 of chest radiographic detectors ($E = 60$ eV) is much higher than of mammographic detectors ($E = 20$ eV) because of the lower α_{air}/ρ_{air} values in (48.3) at higher X-ray photon energies [48.42]. The value of S_0 in a-Se detectors is much lower than in poly-HgI_2 and poly-CZT detectors because of the higher value of $W_\pm$ in a-Se.

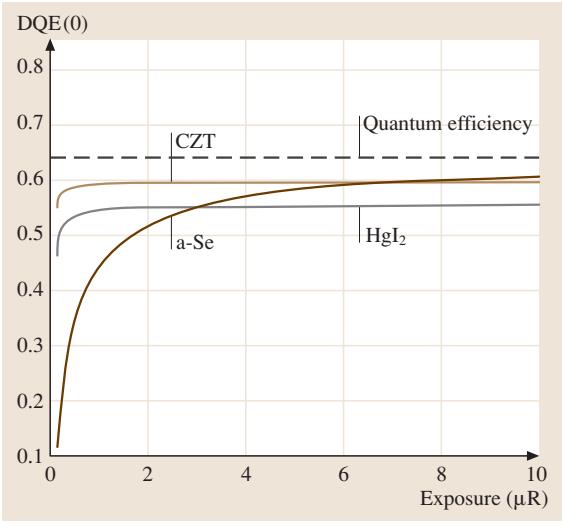

Fig. 48.7 DQE(0) versus X-ray exposure for a-Se, poly-HgI_2, and poly-CZT detectors and for a 60-keV monoenergetic X-ray beam. The electronic noise is 2000 e per pixel. It is assumed that $F = 10\,V/\mu m$ for a-Se, $0.5\,V/\mu m$ for HgI_2 and $0.25\,V/\mu m$ for CZT

48.2.2 Detective Quantum Efficiency

DQE measures the ability of the detector to transfer signal relative to noise from its input to its output. The random nature of image quanta gives rise to random fluctuations in image signals, which contributes to image formation and hence creates random noises. The scattering of image quanta gives rise to image blurring, which is quantified by the MTF(f). Images are partially degraded by various sources of statistical fluctuations that arise along the imaging chain. The relative increase in image noise due to an imaging system as a function of spatial frequency f is expressed quantitatively by DQE(f) which represents the signal-to-noise transfer efficiency for different frequencies of information in an image. DQE(f) is defined as

$$\mathrm{DQE}(f) = \frac{\mathrm{SNR}^2_{out}(f)}{\mathrm{SNR}^2_{in}(f)}\,, \tag{48.5}$$

where SNR_{in} and SNR_{out} are the signal-to-noise ratios (SNR) at the input and output stages of the image detector, respectively. DQE(f) is unity for an ideal detector. For simplicity, we are often interested in measuring DQE($f = 0$) of an imaging detector since it represents the signal quality degradation due to the signal and noise transfer characteristics of the system without considering signal spreading.

The random nature of charge-carrier trapping (i. e. incomplete charge collection) in the photoconductor layer creates fluctuations in the collected charge and hence creates additional noise. Thus carrier trapping degrades signal-to-noise performance of the image and reduces the DQE. Recently, *Kabir* and *Kasap* [48.45]

have examined the effects of charge-carrier trapping on the DQE(0) of an a-Se detector by considering depth-dependent conversion gain and depth-dependent charge-collection efficiency in the cascaded-linear-system model [48.46, 47]. In this section, the DQE(0) model of *Kabir* and *Kasap* [48.45] is applied to potential photoconductive detectors such as a-Se, poly-HgI_2 and poly-$Cd_{0.95}Zn_{0.05}Te$ detectors for fluoroscopic applications to study and compare their DQE(0) performance.

Figure 48.7 shows DQE(0) as a function of X-ray exposure for a-Se, HgI_2, and CZT detectors for a 60-keV X-ray beam. The X-ray exposure (X) is varied from 0.1 μR to 10 μR, which is the range of X-ray exposure for fluoroscopic applications. We assume that the pixel area, $A = 200\,\mu m \times 200\,\mu m$, and the effective fill factor is 1.0 for all types of photoconductors. The average E is 60 keV and the additive electronic noise (N_e) is assumed to be 2000 electrons per pixel. The following transport and operating parameters are used in Fig. 48.7: for a-Se detectors, $L = 1000\,\mu m$, $F = 10\,V/\mu m$, $W_{\pm} \approx 43\,eV$, $\mu_e\tau_e = 10^{-6}\,cm^2/V$ and $\mu_h\tau_h = 10^{-5}\,cm^2/V$; for HgI_2 detectors, $L = 260\,\mu m$, $F = 0.5\,V/\mu m$, $W_{\pm} = 5\,eV$, $\mu_e\tau_e = 6\times10^{-6}\,cm^2/V$ and $\mu_h\tau_h = 10^{-7}\,cm^2/V$; and for CZT detectors, $L = 270\,\mu m$, $F = 0.25\,V/\mu m$, $W_{\pm} = 5\,eV$, $\mu_e\tau_e = 2\times10^{-4}\,cm^2/V$ and $\mu_h\tau_h = 3\times10^{-6}\,cm^2/V$. The radiation-receiving electrode is biased positively for a-Se detectors and negatively for HgI_2 and CZT detectors. $\Delta \approx 0.98$ is for all photoconductors. $\eta = 1 - \exp(-1/\Delta) \approx 0.64$ is the maximum achievable DQE(0) if all the liberated charges are collected.

The DQE for the CZT detector is relatively unchanged over the whole exposure range due to a large conversion gain (low $W_{\pm}$) and high charge-collection efficiency (good transport properties). The DQE for a-Se detectors is small at low exposures because of its relatively low conversion gain and is controlled by the added electronic noise. As the X-ray exposure increases, each pixel receives more photons. The relative contribution of electronic noise to the total noise becomes less important and the DQE increases. The DQE for HgI_2 detectors is relatively small even at higher exposures because of its low charge-collection efficiency, which gives rise to considerable gain-fluctuation noise. Therefore, both high conversion gain and high charge-collection efficiency are required to improve the DQE performance of an X-ray image detector [48.48]. The conversion gain depends on $W_{\pm}$, which is a material property of the photoconductor. The charge-collection efficiency can be improved by increasing F and improving the $\mu\tau$ products of the carriers. However, increasing F also increases the dark current dramatically in both HgI_2 and CdZnTe detectors. Thus there is a practical limitation on F. An F as high as $20\,V/\mu m$ is achievable in a-Se detectors while keeping the dark current within an acceptable level for X-ray imaging [48.26]. The charge-collection efficiency of a-Se detectors is relatively high because of the high F needed to obtain a reasonable $W_{\pm}$.

48.2.3 Modulation Transfer Function (MTF)

Resolution or resolving power is the ability to record separate images of small objects that are placed very closely together. The overall resolution of a system can be expressed as a convolution of the component resolutions. However, the spatial resolution of an imaging device or a system can also be described in terms of the MTF, which is the relative response of the system as a function of spatial frequency. The MTF of an imaging system can be described as a cascade of several stages where the overall MTF is simply the product of the MTFs of all the individual stages. The MTF(f) is a much more convenient descriptor of spatial response since the resolving power from multiplication is much more easily comprehended than convolution. The overall MTF (or presampling MTF) of an image detector can be expressed as,

$$\mathrm{MTF}(f) = \mathrm{MTF_m}(f) \times \mathrm{MTF_a}(f)\,, \qquad (48.6)$$

where $\mathrm{MTF_m}(f)$ is the modulation transfer function of the detector material and $\mathrm{MTF_a}(f)$ is the modulation transfer function associated with the aperture function of the pixel electrodes. $\mathrm{MTF_a}(f)$ arises due to averaging of the signal over a pixel area. If the aperture is square with dimension a, then, $\mathrm{MTF_a}(f)$ will be of the form $\mathrm{sinc}(af)$. The aperture MTF describes how spatial frequencies are passed through the detector elements.

The spatial resolution in direct-conversion AMFPI is high and closer to the aperture function, as compared to phosphor-based AMFPI. Based on current understanding, charge-carrier trapping and reabsorption of K-fluorescent X-ray photons are the two dominant mechanisms responsible for the loss of resolution [48.48] in direct-conversion AMFPI. Some of the K-fluorescent X-ray photons may be reabsorbed at different points within the detector volume from the primary X-ray-photon interaction point. This creates a lateral spreading of signal and a loss of resolution. The loss of resolution due to fluorescence reabsorption is maximum (although not very substantial [48.48]) just above the K-edge of the photoconductor. This effect can

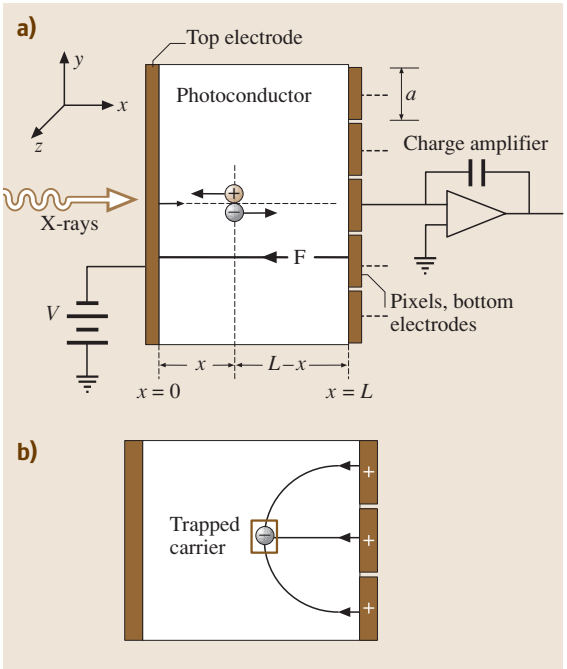

Fig. 48.8 **(a)** A cross section of a direct-conversion pixelated X-ray image detector. **(b)** Trapped carriers in the photoconductor induce charges not only on the central pixel electrode but also on neighboring pixel electrodes, spreading the information and hence reducing spatial resolution

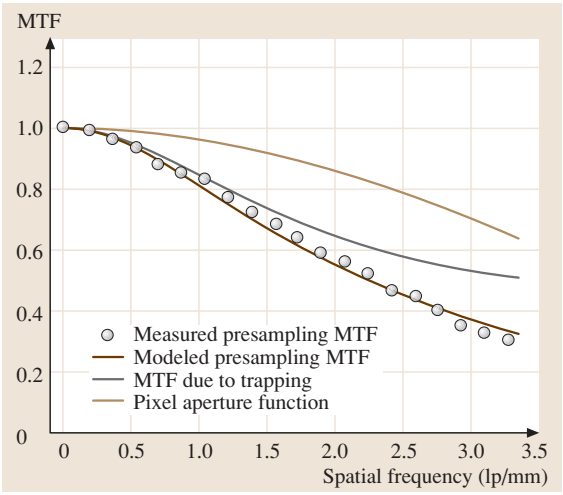

Fig. 48.9 Measured presampling MTF of a polycrystalline CdZnTe detector in comparison with modeled results that included blurring due to charge-carrier trapping in the bulk of the photoconductor. The detector thickness is 300 μm and the pixel pitch is 150 μm. (after Fig. 10 of [48.50])

be ignored when: (i) the incident X-ray photon energy is lower than the K-edge of the photoconductor, or (ii) the mean energy of the X-ray beam and the K-edge occur at widely different energies [48.49]. The charge-carrier trapping has a significant effect on the resolution of these direct-conversion X-ray image detectors [48.36], which will be discussed below.

The direct-conversion AMFPI geometry consists of a photoconductor layer sandwiched between two electrodes; the electrode at one side is a continuous metal plate and the electrode on the other side of the photoconductor is segmented into an array of individual square pixels of size $a \times a$, as shown in Fig. 48.8a. The geometric pixel aperture width in a flat-panel detector is smaller than the pixel pitch (center-to-center spacing between two pixels). However, it has been shown that the effective fill factor (the effective fraction of pixel area used for image-charge collection) of a photoconductive flat-panel detector is close to unity [48.28, 51]. Therefore, the effective pixel aperture width a is virtually identical to the pixel pitch. Some of the X-ray-generated carriers are captured by deep traps in the bulk of the photoconductor during their drift across the photoconductor layer. Suppose that a carrier is trapped in the photoconductor above a particular (central) pixel electrode of a pixellated image sensor. This trapped carrier induces charges not only on the central pixel electrode but also on neighboring pixel electrodes, as shown in Fig. 48.8b, and consequently there is a lateral spread of information and hence a loss of image resolution.

Kabir and *Kasap* [48.36] have developed an analytical expression for the MTF due to distributed carrier trapping in the bulk of the photoconductor and examined the effect of charge-carrier trapping on the resolution of direct-conversion AMFPI. The effect of trapping on MTF increases with decreasing normalized carrier lifetime (i. e., normalized schubweg). Trapping of the carriers that move towards the pixel electrodes degrades the MTF performance, whereas trapping of the other type of carriers, which move away from the pixels, improves the sharpness of the X-ray image.

Figure 48.9 shows the experimental MTF and theoretical fit of a 300-μm-thick positively biased CZT detector exposed to an 80-kVp X-ray beam with 26-mm Al filtration. The experimental data have been extracted from Fig. 10 of [48.50]. The operating $F = 0.25\,\mathrm{V/\mu m}$ and pixel pitch is 150 μm. The Nyquist frequency is 3.3 lp/mm. The dotted line shows the MTF due to the bulk carrier trapping only. The bulk carrier trapping has a significant effect on the

MTF of the detector. As is apparent from Fig. 48.9, there is very good agreement between the model and the experimental data. The best-fit $\mu\tau$ products of electrons and holes are $\mu_e\tau_e = 2.4\times10^{-4}\,\mathrm{cm}^2/\mathrm{V}$ and $\mu_h\tau_h = 3.2\times10^{-6}\,\mathrm{cm}^2/\mathrm{V}$, which are very close to the $\mu\tau$ values reported previously [48.32, 35]. Although the charge-carrier-trapping-limited MTF model has been applied to the CZT sensors, the model can also be applied to other photoconductive (e.g., a-Se and HgI_2) panel X-ray image detectors.

48.3 Conclusion

The principles of operation of a direct-conversion AMFPI for medical applications have been briefly discussed. The charge-transport and imaging properties of some of the potential photoconductors have been critically discussed and compared with the properties of an ideal photoconductor for X-ray image detectors. The various imaging characteristics of photoconductor-based AMFPIs such as the sensitivity (S), detective quantum efficiency (DQE), and resolution in terms of the modulation transfer function (MTF) have also been examined. These characteristics depend critically not only on the photoconductor's charge-transport properties but also on the detector structure, i. e., the size of the pixel and the thickness of the photoconductor. It has been shown that the detector structure in terms of the photoconductor thickness and the pixel size is just as important to the overall performance of the detector as the material properties of the photoconductor itself.

Recent experiments on a-Se detectors indicate that the X-ray-sensitivity of this detector deceases in subsequent exposures. The study of ghosting mechanisms in a-Se-based AMFPI is currently considered as an active research area since the origins of ghosting have not been fully resolved [48.52]. We expect that the ghosting phenomenon may also be present in other photoconductive (e.g., HgI_2, CZT, PbO and PbI_2) detectors, although it has not yet been measured. Long-term stability, and X-ray-induced effects and phenomena are also current research topics.

References

48.1 J. A. Rowlands, J. Yorkston: *Handbook of Medical Imaging*, Vol. 1, ed. by J. Beutel, H. L. Kundel, R. L. Van Metter (SPIE, Washington 2000) Chap. 4 and references therein for the various flat-panel X-ray image sensors

48.2 K. S. Karim, A. Nathan, J. A. Rowlands, S. O. Kasap: IEE Proc.-CDS **150**, 267 (2003)

48.3 V. N. Cooper III, T. Oshiro, C. H. Cagnon, L. W. Bassett, T. M. McLeod-Stockmann, N. V. Bezrukiy: Med. Phys. **30**, 2614 (2003)

48.4 D. C. Hunt, O. Tousignant, J. A. Rowlands: Med. Phys. **31**, 1166 (2004)

48.5 L. E. Antonuk, J. M. Boudry, Y. El-Mohri, W. Huang, J. H. Siewerdsen, J. Yorkston, R. A. Street: Proc. SPIE **2432**, 216 (1995)

48.6 J. Chabbal, C. Chaussat, T. Ducourant, L. Fritsch, J. Michaïlos, V. Spinnler, G. Vieux, M. Arques, G. Halm, M. Hoheisel, H. Horbaschek, R. Schulz, M. Spahn: Proc. SPIE **2708**, 499 (1996)

48.7 J. A. Rowlands, S. O. Kasap: Phys. Today **50**, 24 (1997)

48.8 O. Tousignant, M. Choquette, Y. Demers, L. Laperrière, J. Leboeuf, M. Honda, M. Nishiki, A. Takahashi, A. Tsukamoto: Proc. SPIE **4682**, 503 (2002)

48.9 S. O. Kasap, J. A. Rowlands: *Optoelectronics and Photonics: Principles and Practices* (Prentice-Hall, Upper Saddle River, New Jersey 2001)

48.10 S. O. Kasap, J. A. Rowlands: IEE Proc.-CDS **149**, 85 (2002)

48.11 S. O. Kasap: *Handbook of Imaging Materials*, ed. by A. S. Diamond (Marcel Dekker, New York 1991) Chap. 9

48.12 S. O. Kasap, J. A. Rowlands: Proc. IEEE **90**, 591 (2002)

48.13 F. Greuter, G. Blatter: Semicond. Sci. Technol. **5**, 111 (1990)

48.14 A. Zuck, M. Schieber, O. Khakhan, Z. Burshtein: IEEE Trans. Nuclear Sci. **50**, 991 (2003)

48.15 S. Tokuda, H. Kishihara, S. Adachi, T. Sato: Proc. SPIE **5030**, 861 (2003)

48.16 R. A. Street, S. E. Ready, K. Van Schuylenbergh, J. Ho, J. B. Boyec, P. Nylen, K. Shah, L. Melekhov, H. Hermon: J. Appl. Phys. **91**, 3345 (2002)

48.17 S. Tokuda, H. Kishihara, S. Adachi, T. Sato: J. Mater. Sci. Mater. Electron. **15**, 1 (2004)

48.18 M. Simon, R. A. Ford, A. R. Franklin, S. P. Grabowski, B. Mensor, G. Much, A. Nascetti, M. Overdick, M. J. Powell, D. U. Wiechert: Proc. SPIE **5368**, 188 (2004)

48.19 S. O. Kasap, K. V. Koughia, B. Fogal, G. Belev, R. E. Johanson: Semiconductor **14**, 816 (2003)
48.20 I. M. Blevis, D. C. Hunt, J. A. Rowlands: J. Appl. Phys. **85**, 7958 (1999)
48.21 M. F. Stone, W. Zhao, B. V. Jacak, P. O'Conner, B. Yu, P. Rehak: Med. Phys. **29**, 319 (2002)
48.22 S. O. Kasap: J. Phys. D: Appl. Phys. **33**, 2853 (2000)
48.23 W. Que, J. A. Rowlands: Phys. Rev. B **51**, 10 500 (1995)
48.24 E. Fourkal, M. Lachaine, B. G. Fallone: Phys. Rev. B **63**, 195 204 (2001)
48.25 D. Mah, J. A. Rowlands, J. A. Rawlinson: Med. Phys. **25**, 444 (1998)
48.26 B. Polischuk, Z. Shukri, A. Legros, H. Rougeot: Proc. SPIE **3336**, 494 (1998)
48.27 M. Choquette, Y. Demers, Z. Shukri, O. Tousignant, K. Aoki, M. Honda, A. Takahashi, A. Tsukamoto: Proc. SPIE **4320**, 501 (2001)
48.28 D. C. Hunt, O. Tousignant, Y. Demers, L. Laperrière, J. A. Rowlands: Proc. SPIE **5030**, 226 (2003)
48.29 M. Schieber, A. Zuck, M. Braiman, J. Nissenbaum, R. Turchetta, W. Dulinski, D. Husson, J. L. Riester: IEEE Trans. Nucl. Sci. **NS-44**, 2571 (1997)
48.30 M. Z. Kabir, S. O. Kasap: Appl. Phys. Lett. **80**, 1664 (2002)
48.31 R. C. Whited, L. Van den Berg: IEEE Trans. Nucl. Sci. **NS-24**, 165 (1977)
48.32 Y. Eisen, A. Shor: Mater. Res. Soc. Symp. Proc. **487**, 129 (1997)
48.33 T. L. Chu, S. S. Chu, C. Ferekides, C. Q. Wu, J. Britt, C. Wang: J. Appl. Phys. **70**, 7608 (1991)
48.34 A. Ruzin, Y. Nemirovsky: J. Appl. Phys. **82**, 4166 (1997)
48.35 J. G. Mainprize, N. L. Ford, S. Yin, E. E. Gordon, W. J. Hamilton, T. O. Tümer, M. J. Yaffe: Med. Phys. **29**, 2767 (2002)
48.36 M. Z. Kabir, S. O. Kasap: J. Phys. D: Appl. Phys. **36**, 2352 (2003)
48.37 G. Zentai, L. Partain, R. Pavlyuchkova, C. Proano, G. Virshup, L. Melekhov, A. Zuck, B. N. Breen, O. Dagan, A. Vilensky, M. Schieber, H. Gilboa, P. Bennet, K. Shah, Y. Dmitriev, J. Thomas: Proc. SPIE **5030**, 77 (2003)
48.38 R. A. Street, S. E. Ready, F. Lemmi, K. S. Shah, P. Bennett, Y. Dmitriyev: J. Appl. Phys. **86**, 2660 (1999)
48.39 A. Brauers, U. Schiebel: *US Patent* (1998) No. 5 729 021
48.40 D. R. Ouimette, S. Nudelman, R. Aikens: Proc. SPIE **3336**, 470 (1998)
48.41 D. C. Hunt, S. S. Kirby, J. A. Rowlands: Med. Phys. **29**, 2464 (2002)
48.42 J. M. Boone: *Handbook of Medical Imaging*, Vol. 1, ed. by J. Beutel, H. L. Kundel, R. L. Van Metter (SPIE, Washington 2000) Chap. 1 and references therein
48.43 M. Z. Kabir, S. O. Kasap: J. Vac. Sci. Tech. A **20**, 1082 (2002)
48.44 M. Z. Kabir, S. O. Kasap: J. Vac. Sci. Tech. A **22**, 975 (2004)
48.45 M. Z. Kabir, S. O. Kasap: J. Phys. D: Appl. Phys. **35**, 2735 (2002)
48.46 M. Rabbani, R. Shaw, R. L. Van Metter: J. Opt. Soc. Am. A **4**, 895 (1987)
48.47 J. G. Mainprize, D. C. Hunt, M. J. Yaffe: Med. Phys. **29**, 976 (2002)
48.48 M. Z. Kabir, S. O. Kasap: IEE Proc.-CDS **150**, 258 (2003)
48.49 W. Que, J. A. Rowlands: Med. Phys. **22**, 365 (1995)
48.50 S. Tokuda, H. Kishihara, S. Adachi, T. Sato, Y. Izumi, O. Teranuma, Y. Yamane, S. Yamada: Proc. SPIE **4682**, 30 (2002)
48.51 G. Pang, W. Zhao, J. A. Rowlands: Med. Phys. **25**, 1636 (1998)
48.52 M. Z. Kabir, M. Yunus, S. O. Kasap, O. Tousignant, H. Mani, P. Gauthier: Proc. SPIE **5745**, 223 (2005)